ELSEVIER

Nuclear Instruments and Methods in Physics Research B 132 (1997) 377–390

NIM B
Beam Interactions with Materials & Atoms

An algorithm for Monte Carlo simulation of coupled electron–photon transport

J. Sempau [a], E. Acosta [b], J. Baró [c], J.M. Fernández-Varea [d], F. Salvat [d,*]

[a] *Institut de Tècniques Energètiques, Universitat Politècnica de Catalunya, Diagonal 647, 08028 Barcelona, Spain*
[b] *Facultad de Matemática, Astronomía y Física, Universidad Nacional de Córdoba, Medina Allende y Haya de la Torre, 5000 Córdoba, Argentina*
[c] *Serveis Científico-Tècnics, Universitat de Barcelona, Martí i Franqués s/n, 08028 Barcelona, Spain*
[d] *Facultat de Física (ECM), Universitat de Barcelona, Societat Catalana de Física (IEC), Diagonal 647, 08028 Barcelona, Spain*

Received 5 September 1996; revised form received 4 June 1997

Abstract

An algorithm for Monte Carlo simulation of coupled electron–photon transport is described. Electron and positron tracks are generated by means of PENELOPE, a mixed procedure developed by Baró et al. [Nucl. Instr. and Meth. B 100 (1995) 31]. The simulation of photon transport follows the conventional, detailed method. Photons are assumed to interact via coherent and incoherent scattering, photoelectric absorption and electron–positron pair production. Photon interactions are simulated through analytical differential cross sections, derived from simple physical models and renormalized to reproduce accurate attenuation coefficients available from the literature. The combined algorithm has been implemented in a FORTRAN 77 computer code that generates electron–photon showers in arbitrary materials for the energy range from ~1 GeV down to 1 keV or the binding energy of the L-shell of the heaviest element in the medium, whichever is the largest. The code is capable of following secondary particles that are generated within this energy range. The reliability of the algorithm and computer code is demonstrated by comparing simulation results with experimental data and with results from other Monte Carlo codes. © 1997 Published by Elsevier Science B.V.

1. Introduction

A reliable description of coupled electron–photon transport is required in a number of fields. Thus, knowledge of the space and energy distributions of characteristic X-rays and bremsstrahlung photons generated by electron beams with energies of a few tens of kilo-electron-volt is essential for quantitative electron probe microanalysis (see e.g. Ref. [1]). Detailed information on electron–photon shower evolution is also required for the design and quantitative use of radiation detectors [2,3]. Demands for accurate radiation transport calculations also arise from radiation dosimetry and radiotherapy [4].

Monte Carlo simulation methods have revealed themselves to be the most adequate tools for describing high-energy electron–photon showers,

---

[*] Corresponding author. Tel.: 34 3 402 11 86; fax: 34 3 402 11 74; e-mail: cesc@ecm.ub.es.

0168-583X/97/$17.00 © 1997 Published by Elsevier Science B.V. All rights reserved.
PII S0168-583X(97)00414-X

and a number of computer codes are currently available (e.g. ETRAN [5], ITS3 [6], EGS4 [7], GEANT [8]). With reference to electron transport, these codes have recourse to multiple scattering theories that allow the simulation of the global effect of a large number of events in a track segment of a given length (step). Following Berger [9], these simulation procedures will be referred to as "condensed" Monte Carlo methods. The multiple scattering theories implemented in condensed simulation algorithms are only approximate and may lead to systematic errors, which can be made evident by the dependence of the simulation results on the adopted step length [10]. For keV electron transport, this drawback can be overcome by using detailed simulation, i.e. by simulating all interactions throughout the history of a particle. Monte Carlo codes for the detailed simulation of electron transport have been developed by a number of authors (e.g. [11–13]). Detailed simulation becomes unfeasible for electron energies above a few hundred keV and, on the other hand, condensed simulation loses validity for energies of the order of 100 keV or less.

In a series of previous papers [14–17], we have described a mixed (class II [9]) algorithm for the simulation of electron and positron transport called PENELOPE (an acronym for PENetration and Energy LOss of Positrons and Electrons). This algorithm combines the condensed simulation of soft events (i.e. those with scattering angle and/or energy loss less than preselected cutoffs) with the detailed simulation of hard events. In Ref. [17] we have shown that PENELOPE gives a reliable description of multiple scattering processes for electrons and positrons with energies above ~1 keV. However, the analysis was limited to low atomic number materials or to low energies, to avoid situations in which the transport of bremsstrahlung photons could be important. To make the algorithm useful also at high energies, it is necessary to properly account for the transport of photons and the generation of secondary radiations.

In this work, a complete general-purpose Monte Carlo code for the simulation of electron–photon showers in arbitrary materials is presented, which combines the mixed electron simulation method of PENELOPE with detailed simulation of photon transport. The algorithm also includes the generation of secondary radiations. We keep the name PENELOPE for the complete code, whose description is accomplished with the present paper. It is applicable in the energy range from 1 keV (or the L-shell ionization energy of the heaviest element in the medium, whichever is the largest) up to ~1 GeV.

In Section 2 we give a summary of the adopted photon interaction model together with details on the simulation of secondary radiations originated by photon interactions. Section 3 is devoted to the generation of secondary radiations by electrons and positrons, which were not accounted for in the electron transport algorithm. The relaxation of atoms ionized by photon interactions is considered in Section 4. The reliability of the complete algorithm is analyzed in Section 5 through a comparison of simulation results with a variety of experimental data and with results from other Monte Carlo simulation codes.

2. Photon interactions

The photon interactions considered in the simulation are coherent (Rayleigh) scattering, incoherent (Compton) scattering, photoelectric absorption and electron–positron pair production. Other interactions, such as nuclear absorption, occur with much smaller probability [18] and can be disregarded for most practical purposes. In this section we describe the differential cross sections (DCS) used to simulate the interactions of unpolarized photons of energy E with a single atom of atomic number Z. The extension to compounds is done by means of the additivity approximation, i.e. the molecular DCS is calculated as the sum of the atomic DCSs of the atoms in the molecule.

The most reliable Monte Carlo codes currently in use (see e.g. Ref. [19] and references therein) incorporate accurate DCSs in the form of numerical tables; this requires the use of extensive databases. We follow an alternative approach and use a set of DCSs given in a closed analytical form so that total cross sections, and attenuation coefficients, can be obtained by a single numerical quadrature.

Furthermore, random sampling from these DCSs can be performed analytically. It may be argued that using analytical *approximate* DCSs, instead of more accurate tabulated DCSs, implies a certain loss of accuracy. To minimize this loss, we have adopted analytical forms that are physically plausible and, moreover, PENELOPE renormalizes them so as to reproduce values of partial attenuation coefficients that are read from the input material data file. As a consequence, the free path between events and the kind of interaction are sampled using total cross sections that are nominally exact; approximations are introduced only in the probability distribution functions and have a very mild effect on the simulation results.

2.1. Coherent (Rayleigh) scattering

The DCS for Rayleigh scattering is given by

$$\frac{\mathrm{d}\sigma_{\mathrm{co}}}{\mathrm{d}\Omega} = r_{\mathrm{e}}^2 \frac{1+\cos^2\theta}{2}[F(q,Z)]^2, \tag{1}$$

where $\mathrm{d}\Omega$ is a solid angle element about the direction defined by the polar and azimuthal scattering angles, θ and ϕ. The quantity r_{e} is the classical electron radius and q is the magnitude of the momentum transfer given by

$$q = 2(E/c)\sin(\theta/2) = (E/c)[2(1-\cos\theta)]^{1/2}. \tag{2}$$

The atomic form factor $F(q,Z)$ is calculated from a simple rational expression given by Baró et al. [20] which approximates the numerical form factors tabulated by Hubbell et al. [21]. Random sampling of the scattering angle in Rayleigh interactions is done by means of a rejection method [20].

2.2. Incoherent (Compton) scattering

The atomic DCS for incoherent scattering is calculated from the relativistic impulse approximation [22], which accounts for electron binding effects and Doppler broadening. The Compton DCS per atom, differential in the energy E' and direction $\Omega \equiv (\theta,\phi)$ of the scattered photon, is expressed as [23]

$$\frac{\mathrm{d}^2\sigma_{\mathrm{in}}}{\mathrm{d}E'\,\mathrm{d}\Omega} = \frac{r_{\mathrm{e}}^2}{2}\left(\frac{E_{\mathrm{C}}}{E}\right)^2\left(\frac{E}{E_{\mathrm{C}}}+\frac{E_{\mathrm{C}}}{E}-\sin^2\theta\right) \times F(p_z)\left(\sum_i Z_i \Theta(E-E'-U_i)J_i(p_z)\right)\frac{\mathrm{d}p_z}{\mathrm{d}E'}, \tag{3}$$

where $\Theta(x)$ ($=1$ if $x>0$, $=0$ otherwise) is the Heaviside step function. Contributions from different atomic electron shells are considered separately. Given an atomic shell i with Z_i electrons and binding energy U_i, the effect of the velocity distribution (Doppler broadening) of the electrons is described through the one-electron Compton profile $J_i(p_z)$. We use approximate analytical Compton profiles [23] such that $J_i(0)$ is the value of the one-electron profile at $p_z = 0$ obtained from the Hartree–Fock orbital [24]. This minimizes the required numerical information and simplifies the random sampling, implying only a small loss of accuracy in the DCS [23] as compared to procedures that make use of tabulated Hartree–Fock profiles (see e.g. Ref. [25]). Notice that, owing to electron binding, only Compton interactions with $E - E' > U_i$ are allowed; the adopted ionization energies U_i are taken from Ref. [26]. The quantity

$$E_{\mathrm{C}} \equiv \frac{E}{1+(E/mc^2)(1-\cos\theta)} \tag{4}$$

is the energy of the Compton line, i.e. the energy of photons scattered in the direction θ by a *free electron at rest*. The argument p_z of the Compton profile is the projection of the initial momentum $\boldsymbol{p}$ of the target electron on the direction of the momentum transfer vector $\boldsymbol{q} \equiv \boldsymbol{k} - \boldsymbol{k}'$, where $\boldsymbol{k}$ and $\boldsymbol{k}'$ denote the momenta of the incident and scattered photons; it is approximately given by

$$p_z = \frac{EE'(1-\cos\theta) - mc^2(E-E')}{c\sqrt{E^2+E'^2-2EE'\cos\theta}}. \tag{5}$$

The factor $F(p_z)$ is defined as

$$F(p_z) = 1 + \frac{cq_{\mathrm{C}}}{E}\left(1+\frac{E_{\mathrm{C}}(E_{\mathrm{C}}-E\cos\theta)}{(cq_{\mathrm{C}})^2}\right)\frac{p_z}{mc}, \tag{6}$$

where q_{C} is the momentum transfer associated to the energy $E' = E_{\mathrm{C}}$ of the Compton line,

$$q_C \equiv \frac{1}{c}\sqrt{E^2 + E_C^2 - 2EE_C\cos\theta}. \qquad (7)$$

Eq. (6) is valid only for small $|p_z|$-values; for $p_z < -2mc^2$ and $p_z > 2mc^2$ we set $F(p_z) = F(-0.2mc)$ and $F(p_z) = F(0.2mc)$, respectively. Because of the approximations introduced, negative values of F may be obtained for large $|p_z|$; in this case, we must set $F = 0$.

Finally, the total (atomic) incoherent cross section is obtained by integrating the DCS, Eq. (3), over E' and Ω using the method described by Brusa et al. [23]. This method, consistently based on the impulse approximation, avoids the limitations of the Waller–Hartree theory, which is frequently used in Monte Carlo simulation, e.g. in ITS3 [6] and in EGS4 [25].

As shown in Ref. [23], the simulation of Compton events according to the DCS (Eq. (3)) with analytical one-electron Compton profiles can be performed by using a purely analytical, exact sampling algorithm which is very fast. This algorithm delivers random values of the energy and scattering angles of the secondary photon and the atomic shell from which the Compton electron is ejected. This electron is assumed to be emitted with initial kinetic energy $E_e = E - E' - U_i$ in the direction of the momentum transfer vector $\mathbf{q}$. Moreover, knowledge of the active electron shell involved permits the simulation of characteristic X-rays and/or Auger electrons emitted in the subsequent de-excitation of the ionized atom, as explained in Section 4 below. Accounting for these characteristic X-rays is important e.g. to reproduce the escape peaks of scintillation or solid state detectors and in simulations of X-ray fluorescence spectroscopy [27] and electron probe microanalysis [1].

2.3. Photoelectric effect

Photoionization of a given shell is only possible when the photon energy E exceeds the corresponding ionization energy; this gives rise to the characteristic absorption edges in the photoelectric cross section $\sigma_{\rm ph}$. The atomic cross sections used in PENELOPE are obtained by interpolation in a table that was generated by using the XCOM program of Berger and Hubbell [28] (see also Ref. [29]). The values in this table, which span the energy range from 1 keV to 1 GeV for the elements $Z = 1$ to 92, are estimated to be accurate to within a few percent for photon energies above 1 keV.

In order to minimize the simulation time and computer memory for compound materials (and also for mixtures) PENELOPE interpolates the inverse attenuation coefficient (i.e. the molecular cross section) instead of the atomic cross sections of the constituent elements. Knowledge of the atomic cross sections is needed only when a photoabsorption event has effectively occurred to determine the element that has been ionized. Atomic cross sections are calculated from

$$\sigma_{\rm ph} = \begin{cases} G_{\rm K}\sigma_{\rm ph}^{\rm H}(E,Z) & \text{if } E > E_{\rm c} \equiv 5(Z+15)\ \text{keV}, \\ \exp\,(A_{\rm s} - B_{\rm s}y + C_{\rm s}y^{-1} + D_{\rm s}y^{-2}) & \\ & \text{if } 1\ \text{keV} < E < E_{\rm c}, \end{cases} \qquad (8)$$

where $G_{\rm K}$ is a Z-dependent parameter, $y \equiv \ln E$ and $A_{\rm s}$, $B_{\rm s}$, $C_{\rm s}$ and $D_{\rm s}$ are parameters which are characteristic of each element and change values at the absorption edges [20]. The function $\sigma_{\rm ph}^{\rm H}(E,Z)$ is the empirical high-energy formula due to Hubbell [18], which yields the correct asymptotic behaviour of the photoelectric cross section ($\sigma_{\rm ph} \propto E^{-1}$) at high energies.

Let us assume that the ith shell has been ionized in the photoabsorption event. The discussion of how the active electron shell is selected is postponed to Section 4. A photoelectron with kinetic energy $E_e = E - U_i$ is then emitted in a direction, relative to that of the absorbed photon, defined by the polar and azimuthal angles θ_e and ϕ_e. We consider that the incident photon is not polarized and, hence, the angular distribution of photoelectrons is independent of ϕ_e, which is uniformly distributed in the interval $(0, 2\pi)$. The polar angle θ_e is sampled from the K-shell cross section derived by Sauter [30] using hydrogenic electron wave functions. Strictly speaking, the Sauter DCS is adequate only for ionization of the K-shell by high-energy photons. Nevertheless, in many practical simulations no appreciable errors are introduced when Sauter's distribution is used to describe any photoionization event, irrespective of the atomic shell and the photon energy. The main reason is that the emitted photoelectron immediately starts to interact with the medium, and its direction of movement is substantially altered after travelling a path length much shorter than the photon attenuation length. On the other hand, when the photon energy exceeds the K-edge, most of the ionizations occur in the K-shell and then the Sauter distribution represents a good approximation for most of the cases of photoabsorption.

2.4. Electron–positron pair production

Pair production is simulated by means of a modified Bethe–Heitler formula [20], which assumes an exponentially screened field and includes Coulomb and low-energy corrections. The DCS for the process in which a photon of energy E creates an electron-positron pair, in which the electron has a kinetic energy $E_- = \epsilon E - mc^2$, is given by

$$\frac{\mathrm{d}\sigma_{\mathrm{pp}}}{\mathrm{d}\epsilon} = \alpha r_e^2 Z[Z+\eta] \times \frac{2}{3}\left[2\left(\frac{1}{2}-\epsilon\right)^2 \phi_1(\epsilon) + \phi_2(\epsilon)\right], \tag{9}$$

where α is the fine-structure constant, the quantity η accounts for the creation of pairs in the field of atomic electrons (triplet production), and $\phi_1(\epsilon)$ and $\phi_2(\epsilon)$ are analytical functions of ϵ and the screening radius, which describes electronic screening [14]. Random values of ϵ are generated by using the analytical sampling method described by Baró et al. [20]. Although the integrated Bethe–Heitler cross section accounts for pair and triplet production, all the events are simulated as if they were pairs. This approximation is justified by the fact that, in triplet production, the recoiling electron has a range that is much smaller than the mean free path of the incident photon.

Actually, the complete DCS for pair production is a function of the directions of the pair of particles. As the final state involves three bodies (the nucleus and the produced pair), the directions of the produced particles cannot be obtained from only their kinetic energies. The directions of movement of the electron (θ_-, ϕ_-) and the positron (θ_+, ϕ_+), relative to the direction of the incident photon, are sampled from the leading term of the expression obtained from high-energy theory [31,32]

$$p(\cos\theta_\pm) = a(1-\beta_\pm \cos\theta_\pm)^{-2}, \tag{10}$$

where a is a normalization constant and

$$\beta_\pm = \frac{\sqrt{E_\pm(E_\pm + 2mc^2)}}{E_\pm + mc^2} \tag{11}$$

is the particle velocity in units of the speed of light c. As the directions of the produced particles and the incident photon are not necessarily coplanar, the azimuthal angles ϕ_- and ϕ_+ of the electron and the positron are sampled both independently and uniformly in the interval $(0, 2\pi)$.

3. Secondary radiations generated by electron interactions

The electron and positron transport algorithm described in Ref. [17] already accounts for the production of delta rays (knock-on electrons). Other secondary radiations resulting from "direct" electron and positron interactions are bremsstrahlung and positron annihilation photons.

3.1. Bremsstrahlung photons

The DCS for bremsstrahlung emission by a fast electron, or positron, with initial kinetic energy E in the field of an atom is a complicated function of the energy loss W, the final direction of the projectile and the direction of the emitted photon [33,34]. The usual practice in Monte Carlo simulation is to sample W from the uni-variate distribution obtained by integrating the DCS over the angular variables. Therefore, PENELOPE generates radiative losses of electrons and positrons from a corrected Bethe–Heitler formula [14], differential in the emitted photon energy W, that includes a Coulomb-correction term (thus going beyond the Born approximation) and screening effects. This approach is comparable to the analytical Davies–Bethe–Maximon–Olsen theory implemented in ITS3 for high-energy bremsstrahlung [6]. The DCS is renormalized to exactly reproduce the radiative stopping power given by the program ESTAR of Berger [35], the present method being basically the same as the renormalization procedure used in EGS4 [7]. With this DCS the generation of W is performed very easily, but information on the angular distributions is completely lost. Angular deflections of the projectile are considered to be accounted for by the elastic scattering DCS and, consequently, the direction of movement of the projectile is kept unaltered in the simulation of radiative events.

Let θ denote the polar angle of the direction of the emitted photon relative to the direction of the emitting particle. The mean value of the polar scattering angle is given approximately by [31]

$$\langle\theta\rangle \simeq \frac{mc^2}{E+mc^2}. \tag{12}$$

In the original EGS4 code [7], the polar scattering angle was set equal to $\langle\theta\rangle$ (i.e. photons were emitted on a cone with axis along the direction of incidence and semiaperture $\langle\theta\rangle$), but a more accurate angular distribution has been implemented by the NRCC group [36].

A simpler, but still realistic, angular distribution can be derived from semiclassical arguments as follows (see e.g. Ref. [37]). Consider that the incident electron is moving in the direction of the z-axis of a reference frame K at rest with respect to the laboratory frame. Let (θ', ϕ') denote the polar and azimuthal angles of the direction of the emitted photon in a reference frame K′ that moves with the electron and whose axes are parallel to those of K. In K′, the angular distribution of the emitted photons can be approximated as (dipole approximation)

$$p_{\mathrm{d}}(\cos\theta') = \tfrac{3}{8}(1+\cos^2\theta'). \tag{13}$$

The direction of emission (θ, ϕ) in K is obtained by means of the Lorentz transformation

$$\cos\theta = \frac{\cos\theta' + \beta}{1+\beta\cos\theta'}, \qquad \phi = \phi', \tag{14}$$

where

$$\beta = \frac{\sqrt{E(E+2mc^2)}}{E+mc^2} \tag{15}$$

is the velocity of the electron in units of the speed of light c. Thus, the angular distribution in K is given by

$$\begin{aligned} p(\cos\theta) &= p_{\mathrm{d}}(\cos\theta')\frac{\mathrm{d}(\cos\theta')}{\mathrm{d}(\cos\theta)} \\ &= \frac{3}{16\pi}\left[1+\left(\frac{\cos\theta-\beta}{1-\beta\cos\theta}\right)^2\right] \\ &\quad \times \frac{1}{\gamma^2(1-\beta\cos\theta)^2} \end{aligned} \tag{16}$$

with $\gamma^2 = 1/(1-\beta^2) = 1 + E/(mc^2)$.

To generate random values of $\cos\theta$, we first sample $\cos\theta'$ from the dipole distribution, Eq. (13), using a composition method and then transform it back to the K frame by using the Lorentz transform (Eq. (14)).

In the high-energy limit $(\gamma \gg 1, \theta \ll 1)$, the semiclassical angular distribution (Eq. (16)) takes the form

$$p(\theta) \approx \frac{3\gamma^2}{2\pi}\frac{1+\gamma^4\theta^4}{(1+\gamma^2\theta^2)^4}\theta, \tag{17}$$

in good agreement with the expression obtained from high-energy theory [31,33]. Below ~1 MeV, Eq. (16) begins to depart from the more accurate partial-wave data tabulated by Kissel et al. [38]. At these low energies, however, multiple scattering of the emitting electrons prevails over the "intrinsic" bremsstrahlung angular distribution, except for thin targets (cf. [36]). In order to check this assumption, we have tested the angular probability distribution function based on the Kirkpatrick–Wiedmann–Statham DCS (see e.g. Ref. [39]), which is closer to Kissel et al. partial-wave DCSs [38] than Eq. (16). Preliminary results are shown in Fig. 1 for 30 keV to 1 MeV electrons at normal incidence on 1-csda-range-thick aluminium slabs. Interaction forcing, a variance-reduction technique (see e.g. Ref. [40]), was applied to get sufficiently small statistical uncertainties in the simulated data. Differences due to the adopted intrinsic angular distribution appear mainly at angles below 30° and decrease with increasing initial electron energy, becoming negligible at 1 MeV.

3.2. Positron annihilation

The description of positron annihilation is similar to the one adopted in the EGS4 code [7]. We

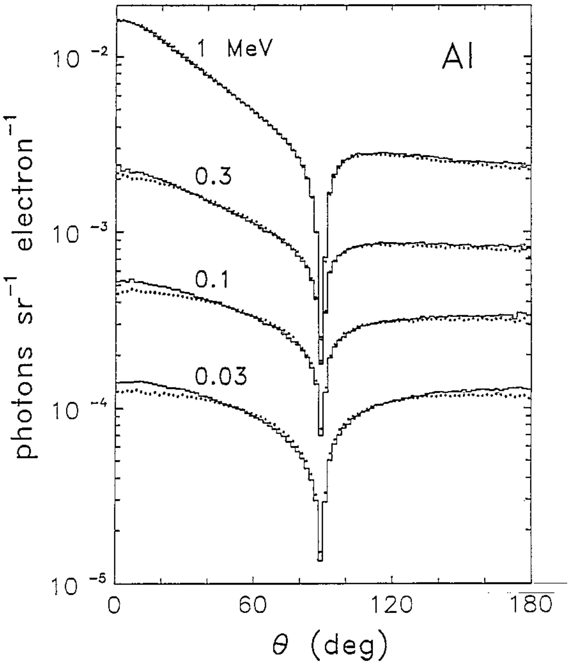

Fig. 1. Angular distributions of bremsstrahlung photons emitted from 1-csda-range-thick aluminium slabs irradiated with electrons of the indicated energies at normal incidence. Histograms are results calculated with the semiclassical expression, Eq. (16). Angular distributions obtained with the Kirkpatrick–Wiedmann–Statham DCS [39] are indicated by dots.

consider that positrons penetrating a medium of atomic number Z with kinetic energy E can annihilate with the electrons in the medium by emission of two photons with energies E_- and E_+, which add to $E + 2mc^2$. Quantities referring to the photon with the lowest energy are denoted by the subscript "–". Each annihilation event is completely characterized by the quantity

$$\zeta \equiv \frac{E_-}{E + 2mc^2}, \tag{18}$$

which takes values in the interval $(\zeta_{\min}, 1/2)$ with

$$\zeta_{\min} = \frac{1}{\gamma + 1 + (\gamma^2 - 1)^{1/2}}. \tag{19}$$

Here, $\gamma = 1 + E/(mc^2)$ is the total energy of the positron in units of its rest energy.

Assuming that the positron moves initially in the direction of the z-axis, from conservation of energy and momentum it follows that the two photons are emitted in directions with polar angles

$$\cos\theta_- = (\gamma^2 - 1)^{-1/2}(\gamma + 1 - 1/\zeta) \tag{20}$$

and

$$\cos\theta_+ = (\gamma^2 - 1)^{-1/2}[\gamma + 1 - 1/(1 - \zeta)], \tag{21}$$

and azimuthal angles ϕ_- and $\phi_+ = \phi_- + \pi$.

The DCS (per electron) for two-photon annihilation is given by [31,7]

$$\frac{d\sigma_{\mathrm{an}}}{d\zeta} = \frac{\pi r_{\mathrm{e}}^2}{(\gamma + 1)(\gamma^2 - 1)}[S(\zeta) + S(1 - \zeta)], \tag{22}$$

where

$$S(\zeta) = -(\gamma + 1)^2 + (\gamma^2 + 4\gamma + 1)\frac{1}{\zeta} - \frac{1}{\zeta^2}. \tag{23}$$

Owing to the axial symmetry of the process, the DCS is independent of the azimuthal angle ϕ_-, which is uniformly distributed on the interval $(0, 2\pi)$. Random values of ζ from the DCS (Eq. (22)) are generated by following the algorithm described by Nelson et al. [7]. As a result of annihilation, two photons with energies $E_- = \zeta(E + 2mc^2)$ and $E_+ = (1 - \zeta)(E + 2mc^2)$ are emitted in the directions given by Eqs. (20) and (21), respectively.

4. Atomic relaxation

Atoms are primarily ionized by photon interactions and by electron or positron impact. There is a fundamental difference between the ionizing effects of photons and of charged particles. A photon is only able to directly ionize a few atoms. In the case of photoabsorption, when the photon energy is larger than the K-shell binding energy, about 80% of photoabsorptions occur in the K-shell, i.e. the resulting ion with a vacancy in the K-shell is highly excited. Incoherent scattering is not as highly preferential, but still the probability that an inner shell is ionized is nearly proportional to the number of electrons in the shell. Conversely, energetic charged particles ionize many atoms along their path and most of the ionizations occur in the less tightly bound atomic shells (or in the conduction band, in the case of metals) so that the ions produced are weakly excited.

Excited ions relax to their ground state by migration of the initial vacancy to outer electron shells, which proceeds through emission of fluorescent X-rays and/or Auger electrons with characteristic energies (see e.g. Perkins et al. [41]). If the initial vacancy is in an outer shell, the emitted radiation is not very energetic and is absorbed in the vicinity of the ion. Consequently, the excitation energy of ions produced by electron and positron impact (and by triplet production) will be assumed to be locally deposited at the interaction site. In the case of photoelectric absorption or Compton scattering, the relaxation of vacancies in inner shells of high-Z elements must be considered in some detail since energetic X-rays and/or electrons are emitted. PENELOPE simulates the emission of characteristic radiation and Auger electrons that result from vacancies produced in a K-shell by photon interactions. Vacancies produced in shells other than the K-shell originate much less energetic radiation. The main effect of this low-energy radiation is to spread out the excitation energy of the ion within the surrounding material. As the direct simulation of the full de-excitation cascade would complicate the code considerably, we simply assume that, when ionization occurs in L or outer shells, the electron is emitted from the parent ion with a kinetic energy equal to the energy deposited by the photon,

$$E_e = \begin{cases} E - E' & \text{in Compton scattering,} \\ E & \text{in photoelectric absorption.} \end{cases} \tag{24}$$

In other words, the whole excitation energy of the ion is taken up by the electron and no fluorescent radiation is simulated. In reality, the emitted electrons have energies less than the values (Eq. (24)) and can be followed by characteristic X-rays, which have mean free paths that are usually much larger than the Bethe range of photoelectrons. By giving an artificially increased initial energy to the electron we allow it to transport energy farther from the ion so as to partially compensate for the neglect of other radiation emitted during the de-excitation cascade.

In the simulation, when the ionization occurs in the K-shell, the electron is ejected with the correct kinetic energy, equal to the deposited energy minus the K-shell ionization energy U_K. In the case of incoherent scattering, the sampling algorithm directly determines the electron shell that is ionized. In the case of photoabsorption, owing to the simplifications we have introduced, we need only determine whether the ionized shell is a K-shell. Evidently, K-shell ionization only happens when $E > U_K$. Then, the probability of absorption in the K-shell is given by

$$P_K(E) = \frac{\sigma_{ph}^K(E)}{\sigma_{ph}(E)}, \tag{25}$$

where $\sigma_{ph}(E)$ and $\sigma_{ph}^K(E)$ are the total atomic photoelectric cross section and the partial cross section for K-shell ionization, respectively. From calculated subshell photoelectric cross sections [42] it is found that $P_K(E)$ is practically independent of the photon energy. It can then be estimated from the K-edge jump ratio,

$$P_K = 1 - \frac{\sigma_{ph}(U_K^-)}{\sigma_{ph}(U_K^+)}, \tag{26}$$

where $\sigma_{ph}(U_K^+)$ and $\sigma_{ph}(U_K^-)$ are values of the photoelectric cross section for energies immediately above and below the K-edge, respectively. Numerical values of this quantity for all the elements have been obtained from the photoelectric cross section tables of Cullen et al. [42]. In the simulation we use the expression

$$P_K = \frac{1 + 8.76 \times 10^{-2} Z - 7.35 \times 10^{-4} Z^2}{0.965 + 0.107 Z - 8.39 \times 10^{-4} Z^2}, \tag{27}$$

which reproduces the numerical values to within 0.6% for $Z > 6$.

To be consistent with the fact that the emission of radiation after ionization of the L and outer shells is disregarded, we only consider characteristic X-rays and Auger electrons emitted in the first stage of the de-excitation cascade, i.e. when the initial vacancy in the K shell is filled by an electron from an outer subshell. Explicitly, the considered emission processes are K-L2, K-L3, K-M2, K-M3, K-N2, K-N3 and K-X radiative transitions and KLX Auger transitions. Here, X denotes the outermost shell with negligible binding energy. The corresponding transition probabilities have been taken from the compilation by Perkins et al. [41]. Although radiative transitions different from the ones indicated above (e.g. K-M4) are also possible, the transition probabilities are exceedingly small (less than 0.01). In the case of Auger emission, we assume that the electron is ejected with the maximum allowed kinetic energy $E_A \simeq U_K - U_{L2}$; this serves to partially compensate for neglecting the subsequent de-excitation cascade.

It is important to bear in mind that the simple approximations adopted in generating characteristic X-rays and Auger electrons set a lower limit to the photon energies for which PENELOPE is applicable. In principle, simulation results are expected to be reliable only for photons with energies larger than the L-shell binding energy (~1 keV for Ni, ~5 keV for I, ~20 keV for U). We also recall that the photoelectric cross section tables [28,29] are limited to $E > 1$ keV, which represents another effective lower limit. A number of practical reasons discouraged us from attempting to extend the photon simulation algorithm to lower energies. Firstly, photon attenuation coefficients at these energies are affected by considerable uncertainties (see e.g. Ref. [43]). Secondly, a consistent simulation of photons with energies below the L edge requires taking into account the generation of X-rays and electrons in this energy range, which can be emitted by heavy atoms after ionization of their L and outer shells. To simulate the de-excitation cascade of ions with a vacancy in these shells, we need the relative probabilities and energies of all possible radiative and non-radiative transitions. These quantities are poorly known; even the L-shell fluorescence yield is uncertain to about 20% (see e.g. refs. [44,41]). Finally, the attenuation length of X-rays with energies of the order of 1 keV (or the L-shell ionization energy, whichever is the larger) is of the order of a few microns, even for light materials such as water and, therefore, for many practical purposes photons with these energies can be assumed to be locally absorbed in the medium.

5. Simulation results

The complete electron–photon shower simulation algorithm has been coded as a FORTRAN 77 subroutine package, tailored to perform most of the simulation work internally. A description of this simulation package, including details of the sampling algorithms, has been published elsewhere [45]. The simulation results reported here are intended to exemplify the kind of situations where PENELOPE can be routinely applied and to demonstrate the reliability of the whole simulation scheme.

A quantity of basic importance in electron-beam dosimetry is the depth–dose distribution, which is defined as the energy deposited per unit mass thickness as a function of depth. Depth–dose distributions for parallel electron beams with energies between 0.1 and 100 MeV impinging normally on elemental materials have been calculated by Tabata et al. [46] using the ITS3 code system. In Fig. 2, simulation results from PENELOPE and ITS are compared with experimental data of Lockwood et al. [47] for 0.5 MeV electrons on uranium. ITS yields a maximum dose somewhat higher than PENELOPE, and our result seems to agree more closely with the experiment. Slight discrepancies between both codes are to be expected for high atomic numbers and/or low energies due to differences in the respective elastic scattering algorithms. Fig. 3 displays depth–dose distributions for 21.2 MeV electrons on polymethylmethacrylate

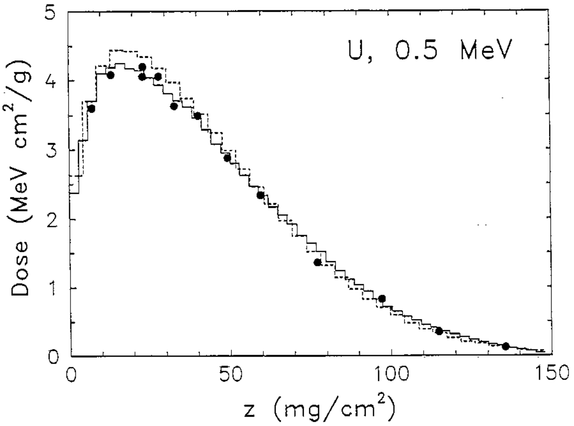

Fig. 2. Depth–dose functions for 0.5 MeV electrons impinging normally on uranium. Continuous and dashed histograms are results from PENELOPE and ITS3 [46], respectively. Dots represent experimental data from Lockwood et al. [47].

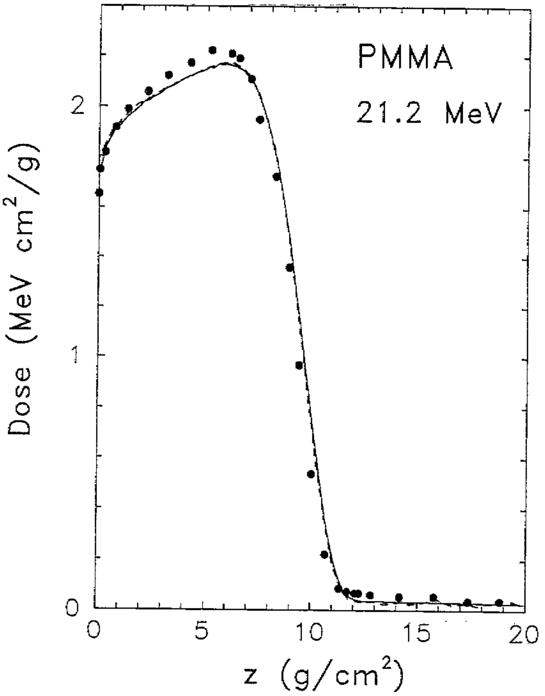

Fig. 3. Depth–dose functions for 21.2 MeV electrons impinging perpendicularly on PMMA. Continuous and dashed curves are results from PENELOPE and ITS3, respectively. The computational speed was about 10 ms/history in both simulations. Dots are experimental data of Harder and Schulz quoted by Berger [48].

(PMMA) computed with PENELOPE and ITS3 together with measurements by Harder and Schulz quoted by Berger [48]. Here, both codes predict depth–dose curves in excellent agreement. This agreement is also remarkable in the radiation tail, which arises from secondary bremsstrahlung photons that propagate deeper than incident electrons.

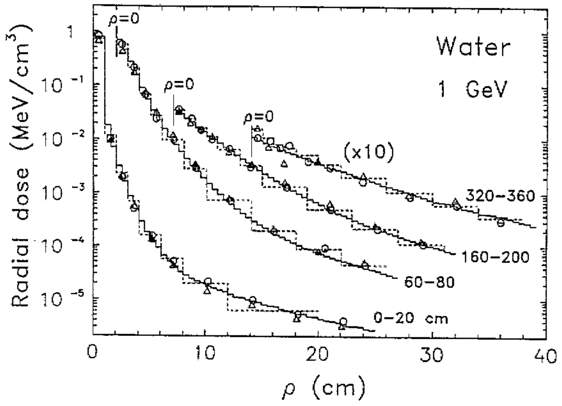

Fig. 4. Radial-dose distributions in water for a 1 GeV electron pencil beam at normal incidence; ρ is the radial distance to the beam. The continuous histograms are results from PENELOPE. Dashed histograms represent experimental data from Crannell et al. [49]. Results from ETRAN and EGS4 are indicated by open triangles and circles, respectively. Each plot represents the radial–dose distribution averaged over the indicated depth interval. Notice that the radial scale of deep layers has been shifted.

In the case of pencil beams, advantage can be taken from the cylindrical symmetry of the spatial dose distribution. The radial-dose distribution is defined as the energy deposited per unit volume, averaged over certain depth and radial intervals, i.e. the volume bins used to tally the dose distribution are hollow cylinders with axis on the incident beam and with given height and inner and outer radii. Fig. 4 compares radial-dose distributions in a semi-infinite water phantom for a 1 GeV electron pencil beam at normal incidence generated by PENELOPE with data measured by Crannell et al. [49] and results from simulations with ETRAN and EGS4 (quoted in Ref. [48]). It is seen that, for this high-energy case, the three codes predict dose distributions with similar accuracy. It is worth pointing out that 1 GeV is the upper end of the energy interval covered by the interaction data base used in PENELOPE. Although the code can be used to simulate showers produced by radiation with higher energy, the simple linear log-log extrapolation adopted to generate cross section tables for energies above 1 GeV may introduce systematic errors in the results that are difficult to predict.

Darriulat et al. [50] published measured efficiencies of a radiation converter for photon energies of 44, 94 and 177 MeV. The converter consists of a lead foil, of variable thickness, on a 0.5 cm thick layer of plastic scintillator. Photons impinged normally on the external surface of the lead foil; an event was counted as a conversion when the energy deposited into the scintillator exceeded 60 keV. In the simulation, we have considered that the scintillator is vinyltoluene-based plastic with 8.5% H and 91.5% C (fractions by weight) and a density of 1.032g/cm^3. The nature of this experiment, and the simplicity of its geometry, makes it particularly well suited to test the reliability of our simulation code. Converter efficiencies calculated with PENELOPE and EGS4 [51] are compared with the measurements of Darriulat et al. in Fig. 5. Our results are seen to agree well with the experimental data. Very likely, discrepancies between PENELOPE and EGS4 arise from an error in this last code, which was pointed out by Andreo [52]. EGS4 assigned initial directions to the generated pair of particles that form the same angle with the direction of the incident photon and this angle was given a value independent of the particle energy. Although this description was far from real, Andreo [52] found that it had no significant effects on the simulation results for low-atomic number materials and energies up to 50 MeV.

As a second example of scintillation detector response, we consider the pulse-height spectrum of a 5″ × 5″ NaI(Tl) detector for a parallel beam of 15 MeV electrons impinging normally on the crystal base. We have simulated this experiment using PENELOPE and ITS3. The Monte Carlo distributions of energy deposited into the crystal have been convoluted with a Gaussian response function (see Fig. 6). The simulated spectra agree closely with each other and with the measurement of Koch and Wyckoff [53] (quoted by Berger [48]).

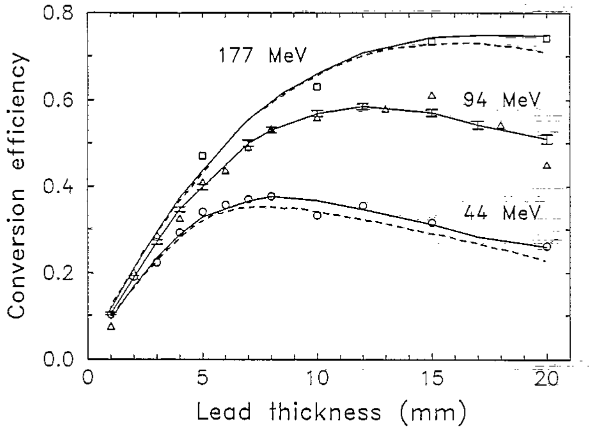

Fig. 5. Efficiency of the radiation converter described in the text as a function of the lead foil thickness. The continuous curves represent results from PENELOPE, dashed lines are results from the EGS4 code (taken from Ref. [51]). Error bars are displayed for the 94 MeV curve. Experimental data of Darriulat et al. [50] are indicated by symbols.

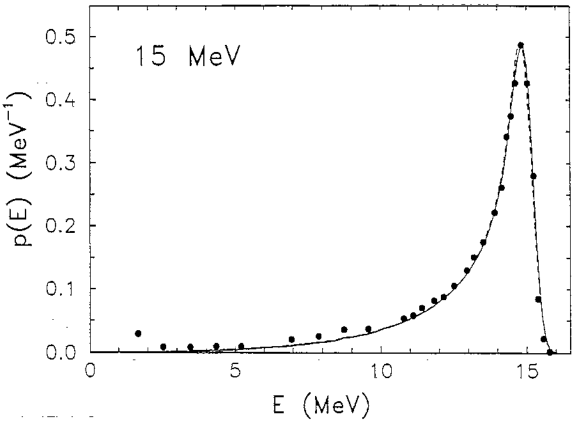

Fig. 6. Pulse-height spectrum of a 5″ × 5″ NaI(Tl) scintillation detector for 15 MeV incident electrons. The continuous and dashed curves are results from PENELOPE and ITS3, respectively (after convolution with a Gaussian response function). Dots are experimental data of Koch and Wyckoff [53] (taken from Ref. [48]).

Work has been initiated to compute the continuous background of electron probe microanalysis (EPMA) spectra using PENELOPE. In EPMA (see e.g. Ref. [1]), the specimen is irradiated with a focused electron beam; incident electrons have kinetic energies of the order of a few tens of keV so that they can produce ionizations of bound atomic electron shells. In the de-excitation of ionized atoms, characteristic X-rays are emitted. Information on the chemical composition of the specimen is obtained by measuring the energy spectrum of photons that leave the irradiated surface of the specimen, which consists of characteristic lines superimposed on a continuous bremsstrahlung background. In practical quantitative analysis, elemental concentrations are inferred from the intensities of characteristic lines in the measured spectra of the specimen and of standards with known compositions. The spectral background contains complementary information that may be valuable for developing standardless analytical methods. Simulations of the continuous component of EPMA spectra of elemental solids have been published recently by Ding et al. [39].

At the energies of interest in EPMA, radiative events have an extremely small stopping effect, i.e. the emission of bremsstrahlung photons with energies larger than ~1 keV is very unlikely. To obtain simulated photon spectra with small enough statistical uncertainties, it is essential to apply interaction forcing [40]. With the aid of this technique, bremsstrahlung spectra for 100 keV electrons incident on a thick tin foil have been generated with PENELOPE. Two angles with respect to the direction of the incident electrons are considered. In Fig. 7(a) and (b), our results are compared with measurements by Placious [54] and equivalent calculations by Berger using ETRAN [48]. A satisfactory agreement is found with both data sets.

Simulations of bremsstrahlung spectra for lower incident electron energies have also been performed. In Fig. 8, the measured EPMA spectrum of copper, generated by a 20 keV electron beam incident normally on the surface of the sample is compared with the result from PENELOPE. The experimental spectrum was obtained by using a SiLi detector with a 6 μm-thick beryllium window. Absorption of photons in the detector window, which is stronger for photons with lower energies, modifies the shape of the spectrum. This absorption effect has been introduced approximately in the calculated spectrum by assuming a purely exponential attenuation in the beryllium window.

It is important to note that PENELOPE has been devised to provide an accurate description of the penetration and slowing down of low-energy electrons and positrons. Electrons with energies of the order of a few tens of keV produce, on average, a very small number of characteristic X-rays by direct impact. As mentioned above, the emission of these X-rays is disregarded in PENELOPE, but

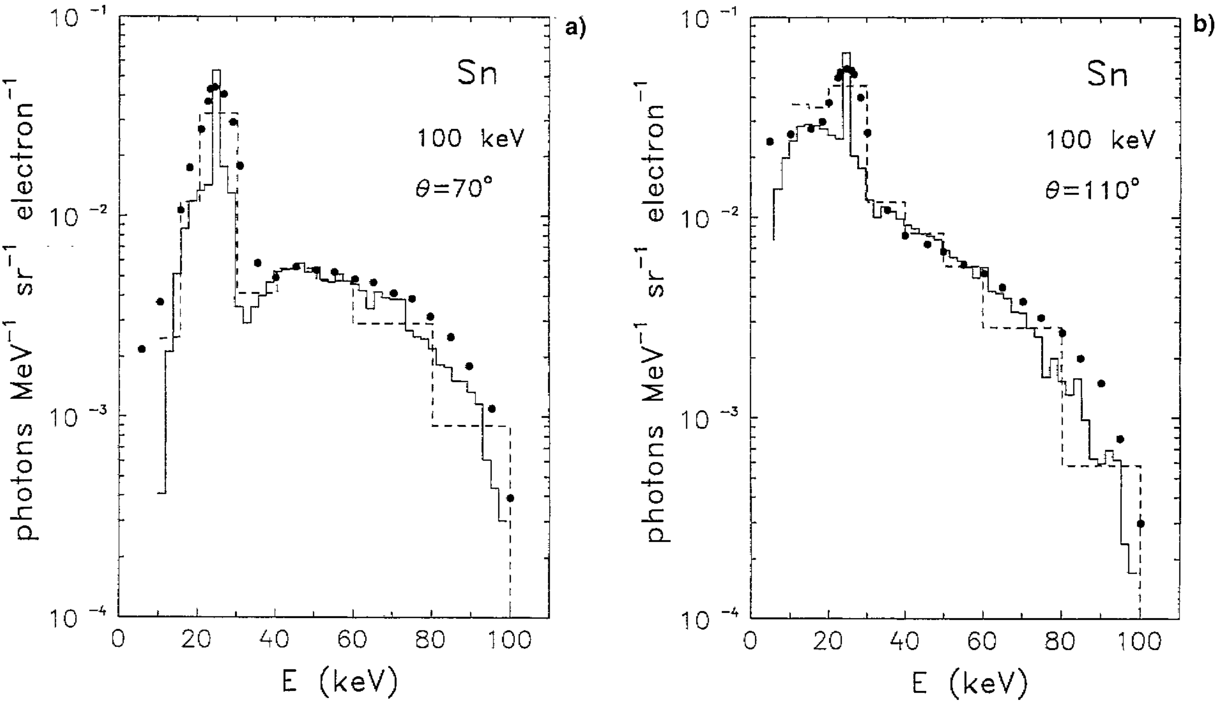

Fig. 7. Bremsstrahlung spectra generated by a 100 keV electron beam incident perpendicularly on a 21.6 mg/cm^2 thick tin foil. The plotted quantity is the number of photons emitted per incident electron, unit solid angle and unit energy in a direction forming an angle of (a) 70° and (b) 110° with that of the electron beam. Continuous histograms: results from PENELOPE. Dashed histograms: calculated by Berger using ETRAN [48]. Dots represent experimental data by Placious [54].

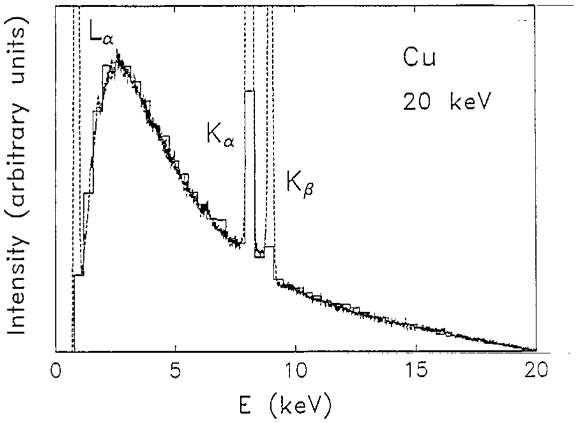

Fig. 8. EPMA spectrum of copper generated with a 20 keV electron beam impinging normally on the sample surface. The photon detector covered a small solid angle about a direction forming an angle of 130° with the electron beam direction.

the effect of ionizing collisions on the projectile is approximately accounted for. Owing to this fact, the simulated bremsstrahlung spectra show characteristic K_α and K_β peaks which are much lower than the experimental ones (see Fig. 8). Actually, the K_α and K_β peaks in the simulated spectra originate from X-rays emitted after photoelectric absorption of bremsstrahlung photons in the K-shell, i.e. bremsstrahlung photons also contribute to the characteristic lines through a fluorescence effect. It is possible to account for the generation of characteristic X-rays by direct electron impact by combining PENELOPE with realistic cross sections for impact ionization of inner-shells. Calculations of K-shell ionization distributions using PENELOPE and semi-empirical ionization cross sections have been described by Llovet et al. [55]. From their results it is a simple matter to compute the characteristic peak intensity caused by direct electron impact, which is missing in the simulated spectra presented here.

In conclusion, we have shown that the interaction models and sampling techniques implemented in PENELOPE provide a realistic description of coupled electron–photon transport in homogeneous media with arbitrary composition and for a wide energy range from about 1 keV (or the L-shell ionization energy if it is larger than this value) up to about 1 GeV.

Acknowledgements

We are indebted to A. Sánchez-Reyes and R. Mayol for valuable suggestions about the code structure. We are also thankful to X. Llovet and A. Riveros for enlightening discussions on simulation and EPMA and for providing us with experimental X-ray spectra, and to L. Carrascosa for performing the ITS3 simulations for Figs. 3 and 6. This work has been partially supported by the Dirección General de Investigación Científica y Técnica (Spain) under contract no.PB92-0801-C02-01.

References

[1] V.D. Scott, G. Love, S.J.B. Reed, Quantitative Electron-Probe Microanalysis, 2nd ed., Ellis Horwood, London, 1995.
[2] F. Titus, Nucl. Instr. and Meth. 89 (1970) 93.
[3] M.J. Berger, S.M. Seltzer, Nucl. Instr. and Meth. 104 (1972) 317.
[4] P. Andreo, Phys. Med. Biol. 36 (1991) 861.
[5] M.J. Berger, S.M. Seltzer, National Bureau of Standards Reports 9836 and 9837, 1968. See also S.M. Seltzer, in: T.M. Jenkins, W.R. Nelson, A. Rindi (Eds.), Monte Carlo Transport of Electrons and Photons, Plenum, New York, 1988, p. 153.
[6] J.A. Halbleib, R.P. Kensek, T.A. Mehlhorn, G.D. Valdez, S.M. Seltzer, M.J. Berger, Report SAND91-1634 Sandia National Laboratories, 1992.
[7] W.R. Nelson, H. Hirayama, D.W.O. Rogers, Stanford Linear Accelerator Center Report SLAC-265, Stanford, 1985.
[8] R. Brun, F. Bruyant, M. Maire, A.C. McPherson, P. Zanarini, CERN Report DD/EE/84-1, Geneva, 1986.
[9] M.J. Berger, in: B. Alder, S. Fernbach, M. Rotenberg (Eds.) Methods in Computational Physics, vol. 1, Academic Press, New York, 1963, p. 135.
[10] A.F. Bielajew, D.W.O. Rogers, Nucl. Instr. and Meth. B 18 (1987) 165.
[11] L. Reimer, E.R. Krefting, National Bureau of Standards Special Publication 460, US Government Printing Office, Washington DC, 1976, p. 45.
[12] S. Ichimura, R. Shimizu, Surf. Science 112 (1981) 386.
[13] J.M. Fernández-Varea, D. Liljequist, S. Csillag, R. Räty, F. Salvat, Nucl. Instr. and Meth. B 108 (1996) 35.
[14] F. Salvat, J.M. Fernández-Varea, Nucl. Instr. and Meth. B 63 (1992) 255.
[15] J.M. Fernández-Varea, R. Mayol, J. Barò, F. Salvat, Nucl. Instr. and Meth. B 73 (1993) 447.
[16] J. Baró, J. Sempau, J.M. Fernández-Varea, F. Salvat, Nucl. Instr. and Meth. B 84 (1994) 465.

[17] J. Baró, J. Sempau, J.M. Fernández-Varea, F. Salvat, Nucl. Instr. and Meth. B 100 (1995) 31.
[18] J.H. Hubbell, H.A. Gimm, I. Øverbø, J. Phys. Chem. Ref. Data 9 (1980) 1023.
[19] T.W. Jenkins, W.R. Nelson, A. Rindi (Eds.), Monte Carlo Transport of Electrons and Photons, Plenum, New York, 1988.
[20] J. Baró, M. Roteta, J.M. Fernández-Varea, F. Salvat, Radiat. Phys. Chem. 44 (1994) 531.
[21] J.H. Hubbell, Wm. J. Veigele, E.A. Briggs, R.T. Brown, D.T. Cromer, R.J. Howerton, J. Phys. Chem. Ref. Data 4 (1975) 471; Erratum: ibid. 6 (1977) 615.
[22] R. Ribberfors, Phys. Rev. A 27 (1983) 3061.
[23] D. Brusa, G. Stutz, J.A. Riveros, J.M. Fernández-Varea, F. Salvat, Nucl. Instr. and Meth. A 379 (1996) 167.
[24] F. Biggs, L.B. Mendelsohn, J.B. Mann, At. Data and Nucl. Data Tables 16 (1975) 201.
[25] Y. Namito, S. Ban, H. Hirayama, Nucl. Instr. and Meth. A 349 (1994) 489.
[26] C.M. Lederer, V.S. Shirley (Eds.), Table of Isotopes, Appendix III. 7th ed., Wiley, New York, 1978.
[27] G.R. Lachance, F. Claisse, Quantitative X-ray Fluorescence Analysis: Theory and Application, Wiley, New York, 1995.
[28] M.J. Berger, J.H. Hubbell, National Bureau of Standards Report NBSIR 87–3597, Washington, 1987.
[29] J.H. Hubbell, S.M. Seltzer, National Institute of Standards and Technology, Report NISTIR 5632, Washington, 1995.
[30] F. Sauter, Ann. Phys. 11 (1931) 454.
[31] W. Heitler, The Quantum Theory of Radiation, Oxford University Press, London, 1954.
[32] J.W. Motz, H.A. Olsen, H.W. Koch, Rev. Mod. Phys. 41 (1969) 581.
[33] H.W. Koch, J.W. Motz, Rev. Mod. Phys. 31 (1959) 920.
[34] Y.S. Tsai, Rev. Mod. Phys. 46 (1974) 815.
[35] M.J. Berger, National Institute of Standards and Technology, Report NISTIR 4999, Washington, 1992.
[36] A.F. Bielajew, R. Mohan, C.-S. Chui, National Research Council of Canada, Report PIRS-0203, Ottawa, 1989.
[37] J.D. Jackson, Classical Electrodynamics, Wiley, New York, 1975.
[38] L. Kissel, C.A. Quarles, R.H. Pratt, At. Data and Nucl. Data Tables 28 (1983) 381.
[39] Z.-J. Ding, R. Shimizu, K. Obori, J. Appl. Phys. 76 (1994) 7180.
[40] A.F. Bielajew, D.W.O. Rogers, in: T.W. Jenkins, W.R. Nelson, A. Rindi (Eds.), Monte Carlo Transport of Electrons and Photons, Plenum, New York, 1988, p. 407.
[41] S.T. Perkins, D.E. Cullen, M.H. Chen, J.H. Hubbell, J. Rathkopf, J. Scofield, Lawrence Livermore National Laboratory, Report UCRL-50400, vol. 30, 1991.
[42] D.E. Cullen, M.H. Chen, J.H. Hubbell, S.T. Perkins, E.F. Plechaty, J.A. Rathkopf, J.H. Scofield, Lawrence Livermore National Laboratory, Report UCRL-50400, vol. 6, rev. 4, parts A and B, 1989.
[43] D.C. Creagh, J.H. Hubbell, International Tables for X-ray Crystallography, vol. C, Kluwer Academic Publishers, Dordrecht, 1992.
[44] J.H. Hubbell, National Institute of Standards and Technology, Report NISTR 89-4144, Washington, 1989.
[45] F. Salvat, J.M. Fernández-Varea J. Baró, J. Sempau, Informes Técnicos Ciemat 799, CIEMAT, Madrid, June 1996.
[46] T. Tabata, P. Andreo, R. Ito, At. Data and Nucl. Data Tables 56 (1994) 105.
[47] G.J. Lockwood, J.A. Halbleib, G.H. Miller, IEEE Trans. Nucl. Sci. NS 25 (1978) 1581.
[48] M.J. Berger, in: T.M. Jenkins, W.R. Nelson, A. Rindi (Eds.), Monte Carlo Transport of Electrons and Photons, Plenum, New York, 1988, p. 183.
[49] C.J. Crannell, H. Crannell, R.R. Whitney, H.D. Zeman, Phys. Rev. 184 (1969) 426.
[50] P. Darriulat, E. Gygi, M. Holder, K.T. McDonald, H.G. Pugh, F. Schneider, K. Tittel, Nucl. Instr. and Meth. 129 (1975) 105.
[51] W.R. Nelson, D.W.O. Rogers, in: T.M. Jenkins, W.R. Nelson, A. Rindi (Eds.), Monte Carlo Transport of Electrons and Photons, Plenum, New York, 1988, p. 287.
[52] P. Andreo, Nucl. Instr. and Meth. B 51 (1990) 107.
[53] H.W. Koch, J.M. Wyckoff, National Bureau of Standards J. Res. 56 (1956) 319.
[54] R. Placious, J. Appl. Phys. 38 (1967) 2030.
[55] X. Llovet, A. Riveros, F. Salvat, Mikrochim. Acta Suppl. 13 (1996) 409.